

Measurement of $\Gamma_{ee} \times \mathcal{B}_{\mu\mu}$ for $\psi(2S)$ meson

V.V. Anashin^a, O.V. Anchugov^a, V.M. Aulchenko^{a,b}, E.M. Baldin^{a,b}, G.N. Baranov^{a,c}, A.K. Barladyan^a, A.Yu. Barnyakov^{a,b}, M.Yu. Barnyakov^{a,b}, S.E. Baru^{a,b}, I.Yu. Basok^a, A.M. Batrakov^a, E.A. Bekhtenev^a, A.E. Blinov^{a,b}, V.E. Blinov^{a,b,c}, A.V. Bobrov^{a,b}, V.S. Bobrovnikov^{a,b}, A.V. Bogomyagkov^{a,b}, A.E. Bondar^{a,b}, A.R. Buzykaev^{a,b}, P.B. Cheblakov^{a,b}, V.L. Dorohov^{a,c}, S.I. Eidelman^{a,b}, D.N. Grigoriev^{a,b,c}, S.A. Glukhov^{a,b}, S.E. Karnaev^a, G.V. Karpov^a, S.V. Karpov^a, K.Yu. Karukina^{a,c}, D.P. Kashtankin^a, T.A. Kharlamova^a, V.A. Kiselev^a, V.V. Kolmogorov^a, S.A. Kononov^{a,b}, K.Yu. Kotov^a, A.A. Krasnov^a, E.A. Kravchenko^{a,b}, V.N. Kudryavtsev^{a,b}, V.F. Kulikov^{a,b}, G.Ya. Kurkin^{a,c}, I.A. Kuyanov^a, E.A. Kuper^{a,b}, E.B. Levichev^{a,c}, D.A. Maksimov^{a,b}, V.M. Malyshev^a, A.L. Maslennikov^{a,b}, O.I. Meshkov^{a,b}, S.I. Mishnev^a, I.A. Morozov^a, I.I. Morozov^{a,b}, N.Yu. Muchnoi^{a,b}, S.A. Nikitin^a, I.B. Nikolaev^{a,b}, I.N. Okunev^a, A.P. Onuchin^{a,b,c}, S.B. Oreshkin^a, A.A. Osipov^{a,b}, I.V. Ovtin^{a,c}, S.V. Peleganchuk^{a,b}, S.G. Pivovarov^{a,c}, P.A. Piminov^a, V.V. Petrov^a, V.G. Prisekin^{a,b}, O.L. Rezanova^{a,b}, A.A. Ruban^{a,b}, G.A. Savinov^a, A.G. Shamov^{a,b}, D.N. Shatilov^a, D.A. Shvedov^a, B.A. Shwartz^{a,b}, E.A. Simonov^a, S.V. Sinyatkin^a, A.N. Skrinsky^a, A.V. Sokolov^{a,b}, D.P. Sukhanov^a, A.M. Sukharev^{a,b,*}, E.V. Starostina^{a,b}, A.A. Talyshev^{a,b}, V.A. Tayursky^{a,b}, V.I. Telnov^{a,b}, Yu.A. Tikhonov^{a,b}, K.Yu. Todyshev^{a,b}, A.G. Tribendis^a, G.M. Tumaikin^a, Yu.V. Usov^a, A.I. Vorobiov^a, V.N. Zhilich^{a,b}, A.A. Zhukov^a, V.V. Zhulanov^{a,b}, A.N. Zhuravlev^{a,b}

^a*Budker Institute of Nuclear Physics, 11, akademika Lavrentieva prospect, Novosibirsk, 630090, Russia*

^b*Novosibirsk State University, 2, Pirogova street, Novosibirsk, 630090, Russia*

^c*Novosibirsk State Technical University, 20, Karl Marx prospect, Novosibirsk, 630092, Russia*

arXiv:1801.10362v2 [hep-ex] 4 Apr 2018

Abstract

The product of the electronic width of the $\psi(2S)$ meson and the branching fraction of its decay to the muon pair was measured in the $e^+e^- \rightarrow \psi(2S) \rightarrow \mu^+\mu^-$ process using nine data sets corresponding to an integrated luminosity of about 6.5 pb^{-1} collected with the KEDR detector at the VEPP-4M electron-positron collider:

$$\Gamma_{ee} \times \mathcal{B}_{\mu\mu} = 19.3 \pm 0.3 \pm 0.5 \text{ eV}.$$

Adding the previous KEDR results on hadronic and leptonic channels, the values of the $\psi(2S)$ electronic width were obtained under two assumptions: either with the assumption of lepton universality

$$\Gamma_{ee} = 2.279 \pm 0.015 \pm 0.042 \text{ keV}$$

or without it, summing up hadronic and three independent leptonic channels

$$\Gamma_{ee} = 2.282 \pm 0.015 \pm 0.042 \text{ keV}.$$

Keywords: $\psi(2S)$ meson, leptonic width, branching fraction

1. Introduction

The narrow charmonium states are frequently referred to as a hydrogen atom of QCD. Their electronic widths Γ_{ee} are rather well predicted by potential models [1, 2], while the accuracy of the QCD lattice calculations of Γ_{ee} gradually approaches that of the measurements [3]. The total and leptonic widths of a hadronic resonance, Γ and $\Gamma_{\ell\ell}$, describe fundamental properties of the strong potential [4].

Besides, the value of the electronic width of narrow charmonium resonances is required for various sum rules, e.g. for determination of the c -quark mass [5].

An experimental study of the leptonic decays of a narrow charmonium is important by itself and is also required for the determination of its electronic and total widths.

In this paper we present a measurement of the product of the $\psi(2S)$ meson electronic width and its branching fraction to the $\mu^+\mu^-$ pair, $\Gamma_{ee} \times \mathcal{B}_{\mu\mu}$. Such an experiment effectively means a measurement of the area under the resonance curve of the $\psi(2S)$ meson and requires data taking at several center-of-mass (c. m.) energy points or the precise knowledge of the machine energy spread. It is worth noting that the presentation of the result in this form is most suitable for fits performed by the Particle Data Group [6] while taking into account results of different experiments.

A measurement of $\Gamma_{ee} \times \mathcal{B}_{ee}$ for the $\psi(2S)$ meson is much

*Corresponding author

Email address: A.M.Suharev@inp.nsk.su (A.M. Sukharev)

more difficult compared to $\Gamma_{ee} \times \mathcal{B}_{\mu\mu}$ due to a large background from the nonresonant production of e^+e^- pairs, unlike the J/ψ case [7], where the probabilities of leptonic decays are about ten times bigger. Another experimental difficulty relevant for both $\Gamma_{ee} \times \mathcal{B}_{ee}$ and $\Gamma_{ee} \times \mathcal{B}_{\mu\mu}$ measurements is the presence of various $\psi(2S)$ decay modes producing the background which has to be explicitly taken into account.

2. VEPP-4M collider and KEDR detector

The VEPP-4M collider [8] can operate in the broad range of beam energies from 1 to 6 GeV. Its peak luminosity in the $\psi(2S)$ energy region is about $2 \times 10^{30} \text{ cm}^{-2}\text{s}^{-1}$.

One of the main features of the VEPP-4M is the possibility of a precise energy determination. At VEPP-4M the relative accuracy of energy calibration with the resonant depolarization is about 10^{-6} . Between calibrations the energy interpolation in the $\psi(2S)$ energy range has the accuracy of $6 \cdot 10^{-6}$ ($\sim 10 \text{ keV}$) [9].

To monitor the beam energy during data taking, the infrared light Compton backscattering technique [10] is employed (with $50 \div 70 \text{ keV}$ precision in the charmonium region).

The main subsystems of the KEDR detector [11] shown in Fig. 1 are the vertex detector, the drift chamber, the scintillation time-of-flight (ToF) counters, the aerogel Cherenkov counters, the barrel liquid krypton calorimeter, the endcap CsI calorimeter and the three-layer muon system built in the yoke of a superconducting coil generating a field of 0.65 T. The detector also includes a tagging system to detect scattered electrons and study two-photon processes. The on-line luminosity is counted by two independent single-bremsstrahlung monitors.

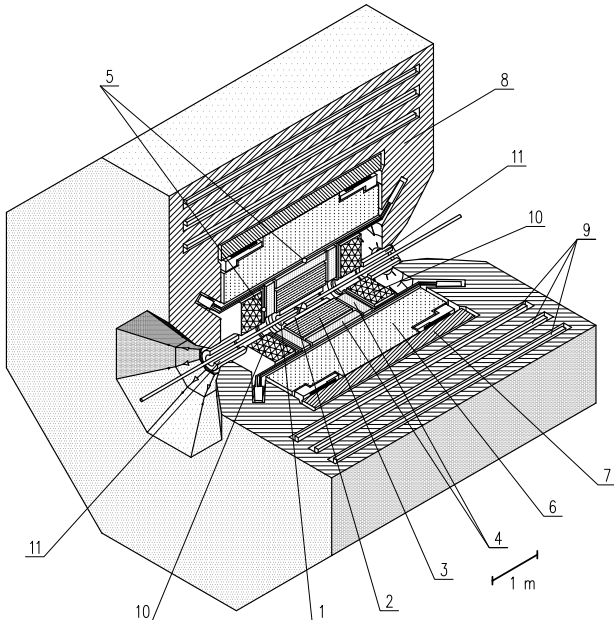


Figure 1: The KEDR detector. 1 – Vacuum chamber, 2 – Vertex detector, 3 – Drift chamber, 4 – Threshold aerogel counters, 5 – ToF counters, 6 – Liquid krypton calorimeter, 7 – Superconducting solenoid, 8 – Magnet yoke, 9 – Muon tubes, 10 – CsI calorimeter, 11 – Compensating superconducting coils.

3. The experiment

Several data sets in the $\psi(2S)$ region were recorded with the KEDR detector since 2004 (Table 1).

Two modes of data taking were employed. In the scan mode, the experimental data were collected at several energy points around the $\psi(2S)$ resonance — near the $\psi(2S)$ cross section peak, at its slopes, and in the continuum slightly below and above the resonance. In the peak/continuum mode, only two energy points were recorded — at the peak and slightly below it. The exact positions of the energy points varied with the data set.

Table 1: KEDR $\psi(2S)$ data sets

Data set	Period	$\int L dt, \text{nb}^{-1}$	σ_w, MeV
Peak/cont. 1	January 2005	358	1.08
Peak/cont. 2	Autumn 2005	222	0.99
Scan 1	Spring 2006	255	0.99
Peak/cont. 3	Spring 2006	631	0.99
Peak/cont. 4	Autumn 2006	701	0.99
Peak/cont. 5	Autumn 2007	1081	1.01
Scan 2	End 2007	967	1.01
Scan 3	Summer 2010	379	1.00
Scan 4	End 2010	2005	0.98

A data sample considered in this analysis corresponds to a total integrated luminosity of more than 6.5 pb^{-1} or about 4×10^6 $\psi(2S)$ decays.

The collider energy spread σ_w required for cross section determination was measured in scans using $e^+e^- \rightarrow \text{hadrons}$ with accuracy of about 2% [9, 12, 13]. The energy spread values measured in the most appropriate scans were used for the peak/continuum data sets, yielding an additional 2% uncertainty [12] due to possible σ_w variation between the data sets.

The detector conditions (trigger parameters, status of subsystems, etc.) varied significantly during the experiment. Various data sets could be considered as partially independent.

The primary trigger signal was provided by a coincidence of two non-adjacent ToF scintillation counters or a localized energy deposition in the barrel calorimeter, for which the hardware energy threshold of approximately 400 MeV has the width about 20%. A veto from the endcap-calorimeter crystals closest to the beam line was used to suppress the machine background in data sets up to the “peak/continuum 4” data set inclusively.

The secondary trigger conditions were suitable to accept two-prong e^+e^- and $\mu^+\mu^-$ events and changed in data sets according to the actual detector state.

During the offline analysis both real and simulated events pass through the software event filter (a so-called “software trigger”) which recalculates a trigger decision using a digitized response of the detector subsystems. This allows to exclude the uncertainties and instabilities of the hardware thresholds.

4. Theoretical $e^+e^- \rightarrow \ell^+\ell^-$ cross section

The analytical expressions for the cross section of the process $e^+e^- \rightarrow \ell^+\ell^-$ with radiative corrections taken into account in the soft-photon approximation were first derived by Ya. A. Azimov et al. in 1975 [14]. With some up-today modifications one obtains in the vicinity of a narrow resonance

$$\left(\frac{d\sigma}{d\Omega}\right)^{ee\rightarrow\mu\mu} = \left(\frac{d\sigma}{d\Omega}\right)_{\text{QED}}^{ee\rightarrow\mu\mu} + \frac{3}{4W^2} (1 + \delta_{\text{sf}}) (1 + \cos^2\theta) \times \left\{ \frac{3\Gamma_{ee}\Gamma_{\mu\mu}}{\Gamma M} \text{Im}f - \frac{2\alpha\sqrt{\Gamma_{ee}\Gamma_{\mu\mu}}}{M} \text{Re}\frac{f}{1-\Pi_0} \right\}, \quad (1)$$

where a correction δ_{sf} follows from the structure function approach of [15]:

$$\delta_{\text{sf}} = \frac{3}{4}\beta + \frac{\alpha}{\pi} \left(\frac{\pi^2}{3} - \frac{1}{2} \right) + \beta^2 \left(\frac{37}{96} - \frac{\pi^2}{12} - \frac{1}{36} \ln \frac{W}{m_e} \right) \quad (2)$$

and

$$f = \frac{\pi\beta}{\sin\pi\beta} \left(\frac{M/2}{-W + M - i\Gamma/2} \right)^{1-\beta} \quad (3)$$

with

$$\beta = \frac{4\alpha}{\pi} \left(\ln \frac{W}{m_e} - \frac{1}{2} \right). \quad (4)$$

Here W is the center-of-mass energy, M , Γ , Γ_{ee} and $\Gamma_{\mu\mu}$ are the resonance mass and its total, electron and muon widths, respectively, θ is the polar angle of outgoing particles, α is the fine-structure constant, m_e is the electron mass. Π_0 represents the vacuum polarization operator with the resonance contribution excluded. The terms proportional to $\text{Im}f$ and $\text{Re}f$ describe the contribution of the resonance and the interference effect, respectively, and, using $\mathcal{B}_{\mu\mu} = \Gamma_{\mu\mu}/\Gamma$, could be rewritten as

$$\left(\frac{d\sigma}{d\Omega}\right)_{\text{res}}^{\mu\mu} \propto \frac{\Gamma_{ee} \times \mathcal{B}_{\mu\mu}}{M} \text{Im}f (1 + \cos^2\theta), \quad (5)$$

$$\left(\frac{d\sigma}{d\Omega}\right)_{\text{int}}^{\mu\mu} \propto \frac{2\alpha\sqrt{\Gamma_{ee} \times \mathcal{B}_{\mu\mu}}}{M} \text{Re}f \frac{1}{1-\Pi_0} (1 + \cos^2\theta),$$

with clearly shown parameter $\Gamma_{ee} \times \mathcal{B}_{\mu\mu}$ and common angular dependence.

The leptonic width definition in Eqs. (1)–(4) implicitly includes vacuum polarization as recommended by PDG: $\Gamma_{\ell\ell} = \Gamma_{\ell\ell}^0 / |1 - \Pi_0|^2$, where $\Gamma_{\ell\ell}^0$ is the lowest-order QED value.

In the e^+e^- channel one has

$$\left(\frac{d\sigma}{d\Omega}\right)^{ee\rightarrow ee} = \left(\frac{d\sigma}{d\Omega}\right)_{\text{QED}}^{ee\rightarrow ee} + \frac{(1 + \delta_{\text{sf}})}{W^2} \left\{ \frac{9}{4} \frac{\Gamma_{ee}^2}{\Gamma M} (1 + \cos^2\theta) \text{Im}f - \frac{3\alpha}{2} \frac{\Gamma_{ee}}{M} \left[\frac{1 + \cos^2\theta}{1 - \Pi_0(s)} - \frac{(1 + \cos\theta)^2}{(1 - \cos\theta)} \frac{1}{1 - \Pi_0(t)} \right] \text{Re}f \right\}, \quad (6)$$

$$s = W^2, t \approx -\frac{s}{2}(1 - \cos\theta),$$

which leads to resonance and interference cross sections expressed with $\mathcal{B}_{ee} = \Gamma_{ee}/\Gamma$ as

$$\left(\frac{d\sigma}{d\Omega}\right)_{\text{res}}^{ee} \propto \frac{\Gamma_{ee} \times \mathcal{B}_{ee}}{M} \text{Im}f (1 + \cos^2\theta),$$

$$\left(\frac{d\sigma}{d\Omega}\right)_{\text{s-int}}^{ee} \propto \frac{2\alpha\sqrt{\Gamma_{ee} \times \mathcal{B}_{ee}}}{M} \text{Re}f (1 + \cos^2\theta) \frac{1}{1 - \Pi_0(s)}, \quad (7)$$

$$\left(\frac{d\sigma}{d\Omega}\right)_{\text{t-int}}^{ee} \propto \frac{2\alpha\sqrt{\Gamma_{ee} \times \mathcal{B}_{ee}}}{M} \text{Re}f \frac{(1 + \cos\theta)^2}{(1 - \cos\theta)} \frac{1}{1 - \Pi_0(t)},$$

where s-int and t-int parts correspond to s- and t-channel interference, respectively. The res and s-int parts have the same angular distribution while t-int has another one.

The accuracy of Eq. (1) and (6) is about 0.1%. Recently it was verified in the work [16] where more precise analytical expressions of the cross sections were suggested.

To compare experimental data with the theoretical cross sections, it is necessary to perform their convolution with a distribution of the total beam energy which is assumed to be Gaussian with an energy spread σ_w :

$$\rho(W) = \frac{1}{\sqrt{2\pi}\sigma_w} \exp\left(-\frac{(W - W_0)^2}{2\sigma_w^2}\right),$$

where W_0 is an average c.m. collision energy. Possible deviation of the distribution from the Gaussian was studied in the analysis [9], and it is taken into account as a systematic uncertainty.

5. Data analysis

5.1. Event selection

Events satisfying the criteria below were selected as $\mu^+\mu^-$:

1. There should be exactly two oppositely charged tracks originating from the beam collision point. Each track should have a corresponding energy deposit in the calorimeter.
2. The software trigger gives a positive decision.
3. Polar θ and azimuthal φ acollinearity is $< 28^\circ$.
4. The energy deposited in the calorimeter for each track should not exceed 700 MeV.
5. There should be not more than one cluster in the calorimeter which is not associated with the tracks, and its energy should not exceed 160 MeV.
6. Both tracks are confirmed by the muon system. Namely, a ‘‘confirmed’’ track should have at least one associated hit in the first or second layer of the muon system.
7. Both tracks should be in the polar angle range of the muon system: $50^\circ < \theta < 130^\circ$.

Additionally, there was a time-of-flight condition to suppress cosmic background. The condition applied to experimental data only. Its efficiency was measured explicitly and discussed in detail in section 6.

e^+e^- events were selected using the following requirements:

1. There should be exactly two oppositely charged tracks originating from the beam collision point. Each track should have a corresponding energy deposit in the calorimeter.
2. The software trigger gives a positive decision.
3. Polar θ and azimuthal φ acollinearity is $< 28^\circ$.
4. The energy deposited in the calorimeter for each track should be greater than 800 MeV.
5. There should be not more than one cluster in the calorimeter which is not associated with the tracks, and its energy should not exceed 160 MeV.
6. Both tracks should be in the polar range of the barrel calorimeter: $45^\circ < \theta < 135^\circ$.

No ToF condition is applied to e^+e^- events.

5.2. Fit procedure

The luminosity was measured using Bhabha scattering with the resonance contribution properly taken into account. In the peak/continuum data sets this implies to use the difference of angular distributions of Bhabha and resonance events. To extract the luminosity, e^+e^- events were divided into equal angular intervals (four by default) of the polar angle θ from 45° to 135° . An "average" $\theta = (\pi - \theta_+ + \theta_-)/2$ was used for each event to take into account possible detector asymmetries. At the i -th energy W_i and the j -th angular interval θ_j , the expected number of $e^+e^- \rightarrow e^+e^-$ events was parameterized as

$$\begin{aligned}
N_{e^+e^-}^{\text{expect}}(W_i, \theta_j) &= \mathcal{L}_i \cdot \sigma_{ee}^{\text{expect}}(W_i, \theta_j), \\
\sigma_{ee}^{\text{expect}}(W_i, \theta_j) &= (\sigma_{\text{res}}^{\text{theor}}(W_i, \theta_j) + \sigma_{\text{s-int}}^{\text{theor}}(W_i, \theta_j)) \cdot \varepsilon_{\text{res}}(\theta_j)|_i \\
&\quad + \sigma_{\text{t-int}}^{\text{theor}}(W_i, \theta_j) \cdot \varepsilon_{\text{int}}(\theta_j)|_i \\
&\quad + \sigma_{\text{cont}}^{\text{sim}}(W_i, \theta_j) \cdot \varepsilon_{\text{cont}}(\theta_j)|_i \\
&\quad + \sigma_{\text{bg}}^{\text{expect}}(W_i, \theta_j),
\end{aligned} \tag{8}$$

where \mathcal{L}_i — integrated luminosity at W_i , σ^{theor} — theoretical cross sections for elastic scattering, resonance and interference, $\varepsilon(\theta_j)|_i$ — detection efficiencies for the j -th angular interval obtained from simulation. The last sum element is the expected contribution of background processes. Each contribution has its own angular distribution and thus its own detection efficiency. The interference angular distribution consists of two parts, one of them being the same as resonance and another with separate $\varepsilon_{\text{t-int}}$.

Since there are no angular θ bins for $\mu^+\mu^-$, the expected number of events at the energy W_i is just:

$$\begin{aligned}
N_{\mu^+\mu^-}^{\text{expect}}(W_i) &= \mathcal{L}_i \cdot \sigma_{\mu\mu}^{\text{expect}}(W_i), \\
\sigma_{\mu\mu}^{\text{expect}}(W_i) &= \varepsilon_{\text{tof}}^{\text{obs}}|_i \times \left((\sigma_{\text{res}}^{\text{theor}}(W_i) + \sigma_{\text{int}}^{\text{theor}}(W_i)) \cdot \varepsilon_{\text{res}}|_i + \right. \\
&\quad \left. + \sigma_{\text{cont}}^{\text{sim}} \cdot \varepsilon_{\text{cont}}|_i + \sigma_{\text{bg}}^{\text{expect}}(W_i) \right),
\end{aligned} \tag{9}$$

which also includes the measured ToF efficiency $\varepsilon_{\text{tof}}^{\text{obs}}$. The resonance and interference for muons have equal angular distributions and thus equal efficiencies.

The products of continuum cross sections and the detection efficiencies $\sigma_{\text{cont}}^{\text{sim}} \cdot \varepsilon_{\text{cont}}$ for both e^+e^- and $\mu^+\mu^-$ are calculated with the simulation program which also accounts for the radiative corrections.

The expected background contribution is a sum of the background decay modes:

$$\sigma_{\text{bg}}^{\text{expect}}(W_i) = \sum_m \sigma_m^{\text{theor}}(W_i) \varepsilon_m|_i, \tag{10}$$

where ε_m — mode m efficiency (individually for each θ bin in the e^+e^- case), and its theoretical cross section $\sigma_m^{\text{theor}}(W)$ is calculated using the mode branching ratio \mathcal{B}_m . Various accelerator and cosmic backgrounds were negligible and therefore were not included in the background contribution.

The products $\Gamma_{ee} \times \mathcal{B}_{\mu\mu}$ and $\Gamma_{ee} \times \mathcal{B}_{ee}$ are free parameters of the fit.

5.3. Simulation

For simulating the nonresonant contribution σ_{cont} in case of e^+e^- scattering we use the BHWIDE [17] generator, MCGPJ [18] and BABAYAGA [19] being the alternatives. The main generator for $\mu^+\mu^-$ scattering was MCGPJ.

The resonant and interference cross sections were simulated using simple generators with proper angular distributions. In this case the initial-state radiative corrections are already taken into account in the expressions (1) and (6). These formulae implicitly involve the branching ratios $\Gamma_{\ell\ell}/\Gamma = \mathcal{B}_{\ell\ell(\text{ray})}$ with the arbitrary number of soft photons emitted. Actual event selection criteria can not be 100% efficient for events with additional photons, therefore the final-state radiation must be simulated explicitly. This was done using the PHOTOS package [20].

The accelerator and cosmic backgrounds as well as various detector noises might overlap useful events, modifying their signature. To take this effect into account, the random trigger (RND) events were recorded during the experiment, and, at the simulation processing stage, simulated events were superimposed with the RND events.

Table 2: $\psi(2S)$ decay background (Bg) modes accounted for in the $\mu^+\mu^-$ analysis. Efficiencies and resulting corrections from each mode vary with the data sets.

Bg mode	$\mathcal{B}_m, \%$	Efficiency, %	Correction, %
$J/\psi\pi^+\pi^-$	34.49	0.03 \div 0.09	2.29 \div 8.94
$J/\psi\pi^0\pi^0$	18.16	0.01 \div 0.02	0.38 \div 0.92
$\gamma\chi_{c0}(1P)$	9.99	< 0.01	0.00 \div 0.05
$\gamma\chi_{c1}(1P)$	9.55	0.03 \div 0.03	0.47 \div 0.92
$\gamma\chi_{c2}(1P)$	9.11	0.02 \div 0.03	0.44 \div 0.69
$J/\psi\eta$	3.36	0.02 \div 0.05	0.17 \div 0.46
e^+e^-	0.79	< 0.01	< 0.01
$\eta c\gamma$	0.34	< 0.01	< 0.01
$\tau^+\tau^-$	0.31	0.05 \div 0.08	0.05 \div 0.07
$J/\psi\pi^0$	0.13	0.10 \div 0.15	0.03 \div 0.05
$p\bar{p}$	0.03	0.01 \div 0.03	< 0.01

Many $\psi(2S)$ decays with $\mu^+\mu^-$ or e^+e^- in the final states could emulate the effect events. For instance, in case of the

cascade decay $\psi(2S) \rightarrow J/\psi X \rightarrow \ell^+ \ell^- X$, when X is undetected or not correctly reconstructed, the similarity could be complete. To subtract such a contribution, simulation has to be used.

Table 2 lists the background decay modes accounted for. These modes have the largest branching ratios. The efficiencies vary notably with the data sets due to significant changes of the detector conditions, the most important one being the turn off several layers of the drift chamber.

Multihadronic and two-photon processes were simulated as well [21]. The corresponding contributions were found to be negligible.

6. Time-of-Flight measurement efficiency

Due to dead time in digitization electronics, the time-of-flight measurement has a significant inefficiency of about 10%. The trigger signals from the time-of-flight system are routed through the separate channels and thus are not affected by this inefficiency.

The condition for each of selected tracks is:

$$|t \times \sin \theta - T_0| \leq 3\sigma_{\text{tof}}, \quad (11)$$

where t and θ — time of flight and polar angle, $T_0 = 2.4$ ns — time of flight for $\psi(2S)$ decay muons in the detector transverse plane, $\sigma_{\text{tof}} = 0.36$ ns — the time resolution. Fig. 2a shows a two-dimensional distribution of the time of flight and the selection criteria.

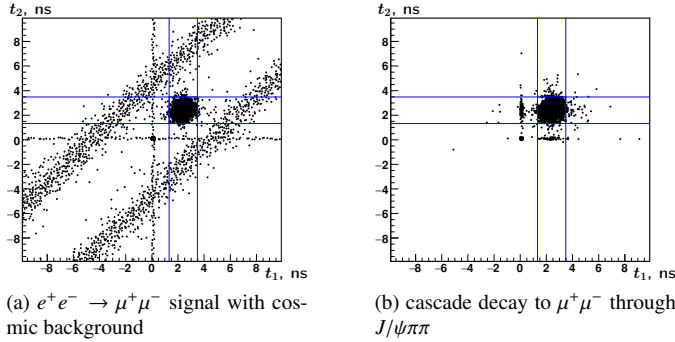


Figure 2: Time-of-flight distribution example for $\mu^+\mu^-$ candidates. $t_{1,2}$ are the times of flight for muon candidate tracks, irrespective to their charge. The selection criteria are shown with a square. Events with lost time are located at $t_{1,2} = 0$. Slant stripes correspond to cosmic events.

The efficiency measurement method (also applied in similar KEDR analysis of J/ψ data [22]) estimates the efficiencies for μ^+ and μ^- separately:

$$\varepsilon_{+/-} = \frac{N^{\text{full}}}{N_{-/+} - N_{-/+}^{\text{bg}}}, \quad N_i^{\text{bg}} = 2 \frac{3\sigma_{\text{tof}}}{\Delta t} L_i^{\text{bg}}, \quad (12)$$

where $N_{+/-}$ — the number of events passing the condition for a corresponding track, N^{full} — that passing the conditions for both tracks. The number of cosmic background events is estimated from the time-of-flight distributions (Fig. 3), where L_i^{bg} is the fitted flat background level, Δt — bin width.

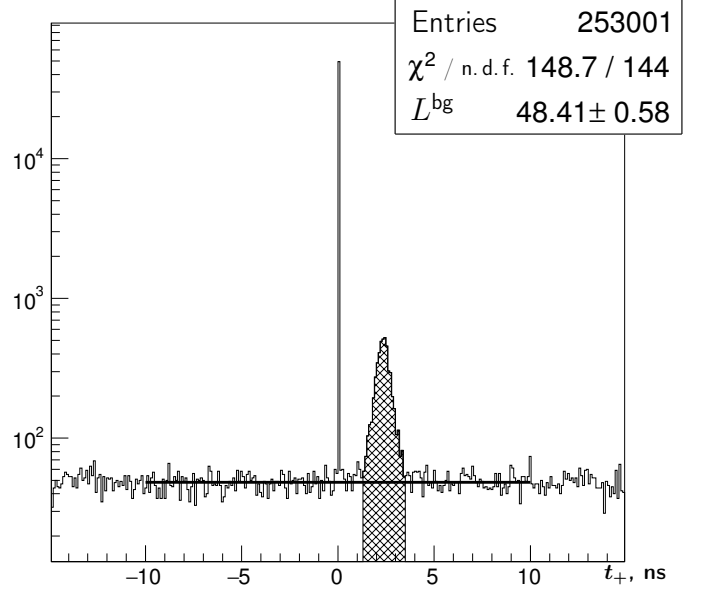


Figure 3: An example of the time of flight (t_+) distribution for μ^+ candidates without the μ^- condition applied. The fitted cosmic background level L^{bg} is shown with the horizontal line, events passing the μ^+ condition are selected by the dashed area.

The total efficiency $\varepsilon_{\text{tof}} = \varepsilon_+ \varepsilon_-$. The uncertainty due to possible correlation of ε_+ and ε_- is less than 0.3% [22].

The results are presented in Table 3. Systematic uncertainties for ε_{tof} were obtained varying conditions of the cosmic background fit and accounting for a possible $\varepsilon_+/\varepsilon_-$ correlation. The values of ε_{tof} were additionally cross-checked using muons from the cascade processes $\psi(2S) \rightarrow J/\psi\pi^+\pi^-$, $\psi(2S) \rightarrow J/\psi\pi^0\pi^0$, where J/ψ decays into $\mu^+\mu^-$ with times of flight very similar to muons from direct $\psi(2S)$ decay (Fig. 2b).

Table 3: Time-of-flight selection criteria efficiency for each data set with statistical and systematic errors.

Data set	ε_{tof} , %
Peak/cont. 1	$85.9 \pm 0.7 \pm 0.9$
Peak/cont. 2	$83.6 \pm 1.0 \pm 1.1$
Scan 1	$84.2 \pm 1.0 \pm 0.5$
Peak/cont. 3	$81.5 \pm 0.6 \pm 0.5$
Peak/cont. 4	$79.8 \pm 0.5 \pm 0.4$
Peak/cont. 5	$86.7 \pm 0.4 \pm 0.4$
Scan 2	$82.9 \pm 0.5 \pm 1.1$
Scan 3	$80.4 \pm 0.8 \pm 0.9$
Scan 4	$81.7 \pm 0.4 \pm 0.9$

7. Systematic uncertainties

The data sets used in the analysis are considered as semi-independent experiments with independent statistical errors but with partially correlated systematic errors. To obtain the final result, the following weighting procedure is applied:

Table 4: Main sources of systematic uncertainties and their relative contributions, %.

Systematic uncertainty source	p/c 1	p/c 2	sc. 1	p/c 3	p/c 4	p/c 5	sc. 2	sc. 3	sc. 4	$\sigma_{\text{syst}}^{\text{corr}}$
1 C. m. energy distribution	1.9	2.7	1.1	2.9	2.2	2.6	1.1	2.9	1.7	0
2 Fixed values of $M_{\psi(2S)}$, $\Gamma_{\psi(2S)}$	0.7	0.6	0.1	0.3	0.7	0.7	0.5	0.2	0.9	0.1
3 Energy measurement	3.1	0.6	< 0.1	1.7	0.3	0.5	0.2	3.8	2.7	< 0.1
4 Bhabha simulation	1.4	1.4	2.2	1.7	1.1	2.1	1.6	2.6	0.9	0.9
5 $\mu^+\mu^-$ scattering simulation	0.2	0.2	0.3	0.2	0.2	0.2	0.2	0.3	0.3	0.2
6 Collinearity cuts	0.8	2.8	2.4	0.8	2.1	1.4	1.5	5.4	1.6	0.8
7 e^+e^- polar angle range	1.1	2.0	1.8	1.0	1.0	1.2	1.6	2.1	1.3	1.0
8 Charge determination	0.6	0.3	0.8	0.6	0.2	1.9	0.1	1.0	0.4	0.1
9 Detector asymmetry	0.9	0.2	0.5	0.9	0.1	0.1	0.2	0.4	0.2	0.1
10 Extra energy deposit cut	1.4	1.2	2.2	0.5	1.0	0.6	2.2	1.7	1.6	0.5
11 Muon system cut	2.5	2.7	2.2	0.6	0.3	0.5	0.6	0.7	< 0.1	0
12 ABG thresholds	0.3	0.7	0.5	0.1	0.3	—	—	—	—	0.1
13 Calo trigger thresholds	0.1	0.1	0.2	0.1	< 0.1	0.4	0.5	0.4	0.2	< 0.1
14 RND trigger application	0.2	0.1	< 0.1	< 0.1	< 0.1	0.3	0.1	0.9	0.3	< 0.1
15 FSR accounting	0.4	0.4	0.4	0.4	0.4	0.4	0.4	0.4	0.3	0.3
16 e^+e^- events θ binning	0.6	0.2	0.6	0.5	0.5	0.3	0.1	0.4	0.3	0.1
17 ToF measurement efficiency	1.9	2.5	1.5	1.2	0.8	0.9	2.8	2.7	2.3	0.8
18 Trigger efficiency	0.9	< 0.1	0.2	0.1	0.1	0.1	0.2	0.1	0.1	< 0.1
19 Theoretical accuracy	0.1	0.1	0.1	0.1	0.1	0.1	0.1	0.1	0.1	0.1
Sum in quadrature	5.7	6.2	5.4	4.4	3.7	4.5	4.7	8.7	4.9	1.9

$$\begin{aligned}
 \langle \Gamma_{ee} \times \mathcal{B}_{\mu\mu} \rangle &= \sum w_i \times (\Gamma_{ee} \times \mathcal{B}_{\mu\mu})_i, \\
 \sigma_{\text{stat}}^2 &= \sum w_i^2 \times \sigma_{\text{stat},i}^2 \\
 \sigma_{\text{syst}}^2 &= \sum w_i^2 \times (\sigma_{\text{syst},i}^2 - \sigma_{\text{syst},0}^2) + \sigma_{\text{syst},0}^2 \\
 w_i &\propto 1/(\sigma_{\text{stat},i}^2 + \sigma_{\text{syst},i}^2 - \sigma_{\text{syst},0}^2),
 \end{aligned} \tag{13}$$

where w_i — i -th measurement weight, accounting for statistical errors and uncorrelated part of systematic errors, $\sigma_{\text{syst},0}^2$ — correlated part of systematic uncertainty.

The determination of the correlated part of systematic errors is not a trivial task, and in most cases we assumed that the correlated part corresponds to the minimal uncertainty in data sets for a given uncertainty source. This leads to the most conservative estimates of the total uncertainty.

Table 4 shows the main sources of systematic uncertainties, their contributions for each data set, correlated parts and sums in quadrature. Below is the explanation for each row of the table.

The contribution of the center-of-mass energy shape (row 1) was obtained varying σ_w according to its uncertainty, which is partially due to non-Gaussian effects (see sections 3 and 4).

To calculate cross sections, the $\psi(2S)$ mass value measured by the KEDR detector [9] was used, while the width was taken from the PDG tables [6]. Varying the mass and width within their errors gives the contribution to the uncertainty of the result (row 2).

To estimate the uncertainty originated from the energy measurement (row 3), the default analysis version using average $\langle W_{\text{run}} \rangle_i$ to compute the cross section $\sigma_i = \sigma(\langle W_{\text{run}} \rangle_i)$ at the i -th

energy point was compared to that with an average cross section $\sigma_i = \langle \sigma(W_{\text{run}}) \rangle_i$.

The systematic uncertainty from e^+e^- -scattering simulation was estimated comparing results obtained with the default generator BHWIDE and alternative generators BABAYAGA and MCGPJ. The $\mu^+\mu^-$ continuum cross section is calculated by the MCGPJ generator with statistical precision of $\approx 0.1\%$, the systematic part $\lesssim 0.2\%$ is the declared precision of the MCGPJ generator. Estimations of these systematic uncertainties are presented in the rows 4 and 5.

The ‘‘collinearity cut’’ contribution to the resulting uncertainty (row 6) was estimated by varying the cuts: reducing the acollinearity limit from 28° to 10° and imposing global polar angle limits just on one track instead of both.

A minimal polar angle limit for e^+e^- events varied in the interval $[-5^\circ, +5^\circ]$ from its default value of 45° . Maximal change of the result with such variations is shown in the row 7.

The charge misidentification impact (row 8) was studied using a special version of track reconstruction allowing incorrect determination of one or two track charges.

In the standard fit version, the ‘‘average’’ θ angle (see subsection 5.2) was used to build distributions over polar angle. The ‘‘detector asymmetry’’ (row 9) error comes from comparison of results obtained with angles of positively (θ_+) or negatively (θ_-) charged tracks separately.

The requirement on calorimeter clusters unattached to any track was varied widely, allowing two extra clusters instead of one, and limiting the extra energy at 90 and 200 MeV instead of default 160 MeV. The maximal change of the result is presented in the row 10.

The muon system cut contribution (row 11) was checked al-

lowing one track without muon system confirmation. To avoid extra background, an additional cut on particle momenta has to be imposed.

The antibackground (ABG) trigger veto was in effect in several early data sets (see section 3). ABG energy thresholds in software trigger varied approximately from -50% to +50% to estimate the influence on the result uncertainty (row 12).

The calorimeter trigger thresholds were increased by 25% to estimate the corresponding contribution to the result uncertainty (row 13).

Systematic uncertainties due to RND events usage were estimated by the fluctuations of the result caused by change of a subset of noise and background events applied to the simulation (row 14).

Final-state radiation effect accounted for by the PHOTOS package is about 4%. Its systematic uncertainty is estimated to be of about 10% of the effect, i.e. $\sim 0.4\%$ [20] (row 15).

The result fluctuated slightly when changing the number of θ bins to divide e^+e^- data. The maximal fluctuation for 5, 10, 15, 20 bins (instead of 4 by default) was taken as a contribution to a systematic uncertainty (row 16).

The ToF measurement contribution (row 17) is described separately in section 6.

The trigger efficiency was found to be more than 99.3% for primary trigger and 98.0 \div 99.9% (depending on the data set) for secondary trigger. Their variations in error limits give the contribution to systematic uncertainty (row 18).

Accuracy of the theoretical formulae used (row 19) is expected to be at the level of 0.1% [15].

8. Results and conclusion

Nine data sets recorded by the KEDR detector in the $\psi(2S)$ region were processed, the total number of $\psi(2S)$ being about 4×10^6 . Our results of the measurement for each data set are listed in Table 5.

Table 5: Result and errors (eV) and fit quality for each data set.

Data set	$\Gamma_{ee} \times \mathcal{B}_{\mu\mu}$	σ_{stat}	σ_{syst}	$\chi^2/\text{n. d. f.}$
Peak/cont. 1	20.5	1.2	1.2	2.6/6
Peak/cont. 2	21.5	1.7	1.3	12.6/6
Scan 1	18.9	1.9	1.0	27.0/26
Peak/cont. 3	17.5	0.8	0.8	2.1/6
Peak/cont. 4	20.2	0.8	0.8	6.0/6
Peak/cont. 5	19.3	0.7	0.9	12.2/6
Scan 2	20.9	1.0	1.0	28.4/30
Scan 3	16.1	1.3	1.4	25.0/18
Scan 4	19.3	0.6	0.9	20.5/18

The final average value is:

$$\Gamma_{ee} \times \mathcal{B}_{\mu\mu} = 19.3 \pm 0.3 \pm 0.5 \text{ eV.}$$

Particle Data Group [6] does not list any direct $\Gamma_{ee} \times \mathcal{B}_{\mu\mu}$ measurement. Using PDG numbers for $\Gamma_{ee} = 2.34 \pm 0.04 \text{ keV}$

and $\mathcal{B}_{\mu\mu} = (7.9 \pm 0.9) \times 10^{-3}$, one could get the ‘‘world average’’ of

$$\Gamma_{ee} \times \mathcal{B}_{\mu\mu} = 18.5 \pm 2.1 \text{ eV,}$$

which is in good agreement with our result (Fig. 4). An example of observed $\mu^+\mu^-$ cross section is shown in Fig. 5.

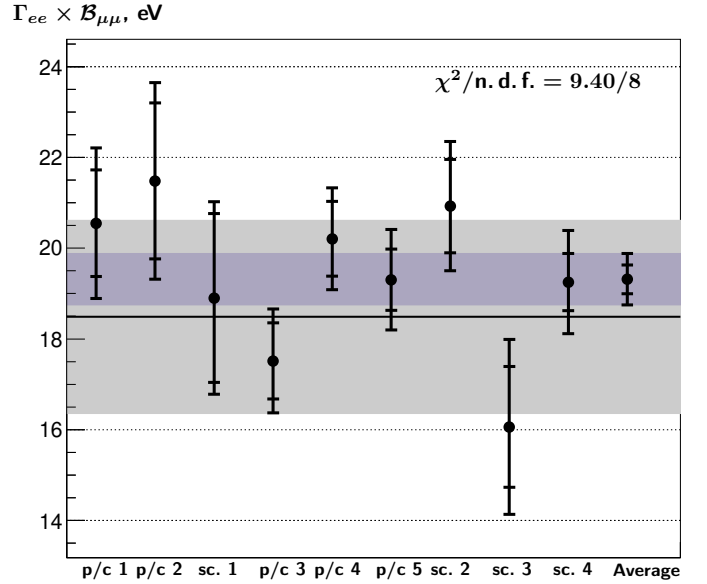


Figure 4: Result on $\Gamma_{ee} \times \mathcal{B}_{\mu\mu}$ for each data set (ticks on the error bars correspond to statistical and total uncertainties) and the averaged result with its total error (the dark gray band). The horizontal line and light gray band indicate the ‘‘world average’’ and its error. The chi-square of the averaging and number of degree of freedom are also shown.

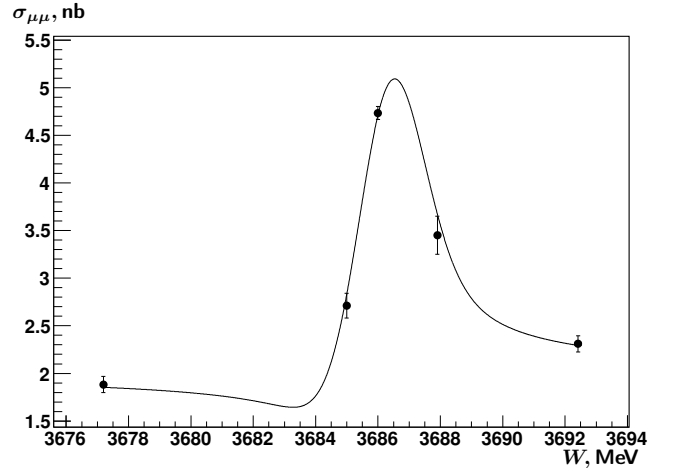


Figure 5: An illustration of the observed $\mu^+\mu^-$ cross section in scan 4.

Combining our $\Gamma_{ee} \times \mathcal{B}_{\mu\mu}$ result with the KEDR measurement of $\Gamma_{ee} \times \mathcal{B}_{\text{hadrons}} = 2.233 \pm 0.015 \pm 0.042 \text{ keV}$ [13] we obtained the following value of the $\psi(2S)$ electronic width:

$$\Gamma_{ee} = 2.279 \pm 0.015 \pm 0.042 \text{ keV}$$

in the assumption of the lepton universality.

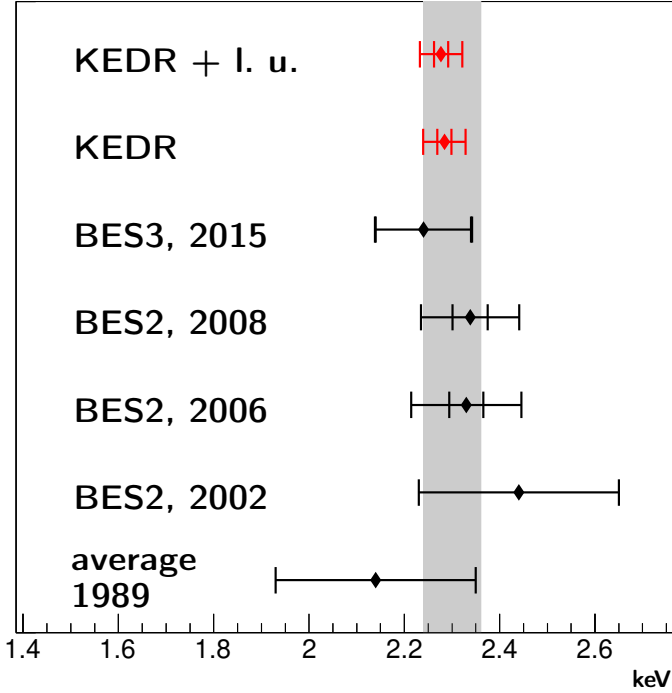


Figure 6: Comparison of $\Gamma_{ee}(\psi(2S))$ measurements. The gray band indicates the current PDG average. Both KEDR values with and without assumption of lepton universality are represented. Total and statistical (where possible) errors are shown.

Although not presented as a result of this work, the $\Gamma_{ee} \times \mathcal{B}_{ee}$ value also comes out of the analysis:

$$\Gamma_{ee} \times \mathcal{B}_{ee} = 21.2 \pm 0.7 \pm 1.2 \text{ eV.}$$

For $\psi(2S)$ the resonance cross section is far too small compared to Bhabha, so the systematic error in the e^+e^- channel is much bigger. Nevertheless, this allows us to calculate the Γ_{ee} value without the lepton universality assumption (the required value of $\Gamma_{ee} \times \mathcal{B}_{\tau\tau} = 9.0 \pm 2.6 \text{ eV}$ is taken from another KEDR measurement [23]):

$$\Gamma_{ee} = 2.282 \pm 0.015 \pm 0.042 \text{ keV.}$$

Our Γ_{ee} values and their comparison with previous results are presented in the Fig. 6. Γ_{ee} uncertainties are dominated by $\Gamma_{ee} \times \mathcal{B}_{\text{hadrons}}$ uncertainties either with the lepton universality assumption or without it.

Acknowledgments

We greatly appreciate the efforts of the staff of VEPP-4M to provide good operation of the complex and the staff of experimental laboratories for the permanent support in preparing and performing this experiment.

The Siberian Branch of the Russian Academy of Sciences Siberian Supercomputer Center and Novosibirsk State University Supercomputer Center are gratefully acknowledged for providing supercomputer facilities [24].

This work was supported by Russian Science Foundation under project N 14-50-00080.

References

References

- [1] A. M. Badalian and I. V. Danilkin, Phys. Atom. Nucl. **72**, 1206 (2009).
- [2] O. Lakhina and E. S. Swanson, Phys. Rev. D **74**, 014012 (2006).
- [3] J. J. Dudek, R. G. Edwards and D. G. Richards, Phys. Rev. D **73**, 074507 (2006).
- [4] N. Brambilla *et al.*, Eur. Phys. J. C **71**, 1534 (2011).
- [5] K. Chetyrkin *et al.*, Theor. Math. Phys. **170**, 217 (2012).
- [6] Particle Data Group, C. Patrignani *et al.*, Chin. Phys. C **40**, 100001 (2016).
- [7] V. V. Anashin *et al.*, Phys. Lett. B **685**, 134 (2010).
- [8] V. V. Anashin *et al.*, Stockholm 1998, EPAC 98*, 400 (1998), Prepared for 6th European Particle Accelerator Conference (EPAC 98), Stockholm, Sweden, 22-26 Jun 1998.
- [9] V. V. Anashin *et al.*, Physics Letters B **749**, 50 (2015).
- [10] E. V. Abakumova *et al.*, Nucl. Instr. Methods Phys. Res., Sect. A **744** (2014).
- [11] V. V. Anashin *et al.*, Phys. of Part. and Nucl. **44**, 657 (2013).
- [12] V. M. Aulchenko *et al.*, Phys. Lett. B **573**, 63 (2003).
- [13] V. V. Anashin *et al.*, Phys. Lett. B **711**, 280 (2012).
- [14] Y. I. Asimov *et al.*, JETP Lett. **21**, 172 (1975).
- [15] E. A. Kuraev and V. S. Fadin, Sov. J. Nucl. Phys. **41**, 466 (1985).
- [16] X. Y. Zhou, Y. D. Wang and L. G. Xia, Chin. Phys. C **41**, 083001 (2017).
- [17] S. Jadach, W. Płaczek and B. F. L. Ward, Phys. Lett. B **390**, 298 (1997).
- [18] A. B. Arbuzov, G. V. Fedotov, F. V. Ignatov, E. A. Kuraev and A. L. Sibidanov, Eur. Phys. J. C **46**, 689 (2006).
- [19] C. M. Carloni Calame *et al.*, Nucl. Phys. B - Proceedings Supplements **131**, 48 (2004).
- [20] E. Barberio and Z. Was, Comput. Phys. Commun. **79**, 291 (1994).
- [21] V. A. Tayursky, J. Phys.: Conf. Ser. **798**, 012153 (2017).
- [22] V. M. Aulchenko *et al.*, Phys. Lett. B **731**, 227 (2014).
- [23] V. V. Anashin *et al.*, JETP Lett. **85**, 347 (2007).
- [24] A. Adakin *et al.*, J. Phys.: Conf. Ser. **396**, 042064 (2012).